ADVANCED OPTICAL MATERIALS
www.advopticalmat.de

Accessible Nearfields by Nanoantennas on Nanopedestals for Ultrasensitive Vibrational Spectroscopy

*Arif E. Cetin, Dordaneh Etezadi, and Hatice Altug**

Nanoplasmonics have been exploited for a variety of applications ranging from optoelectronic devices to biodetection systems.[1–21] Techniques including surface-enhanced fluorescence, infrared absorption (SEIRA), Raman scattering (SERS) and refractive index (RI) based sensing employ distinct plasmonic properties of metallic structures to achieve ultra-high sensitivities.[22–41] In particular, surface enhanced absorption spectroscopy in Mid-infrared (Mid-IR) spectral range is of great interest as it provides direct access to rich vibrational information of most organic molecules and enables investigation of unique structural characteristics of biosamples. Mid-IR spectroscopy has been used as a label-free identification tool for obtaining fingerprints of molecules and complex macromolecules, e.g., proteins and lipids.[42] However, the sensitivity of Mid-IR spectroscopy techniques is fundamentally limited by the dependence of the signal on the path length based on Beer's law. This limitation can be overcome by the use of surface enhanced IR absorption spectroscopy (SEIRA).[43] Employing plasmonic structures enabling strong coupling between electromagnetic fields and the biomolecules of interest, SEIRA can provide orders of magnitude signal enhancement compared to the traditional spectroscopy techniques and enable ultrasensitive detection of biosamples including very thin protein monolayers.[23,42] Recently, integration of engineered plasmonic substrates with microfluidics has been successfully demonstrated for in-situ, real-time and ultrasensitive spectroscopy of biomolecular interactions.[43] Furthermore, nearfield measurement approaches based on plasmonic tips have been applied for spectroscopic characterization of biosamples with nanoscale spatial resolution.[44,45]

Recent advancements in SEIRA have demonstrated unique opportunities in bioapplications, however its development for non-destructive, label-free and highly sensitive spectroscopy as well as high-resolution microscopy, is still at its infancy. Significant research have focused on investigation of novel nanostructure designs to advance performance of SEIRA techniques by increasing their sensitivity. Specifically, for applications associated with extremely low signal levels, such as biosamples with ultralow analyte concentration, single cell monitoring and single molecule detection, high signal-to-noise ratio (SNR) is required for reliable spectroscopic analysis within minimum detection time. Under such circumstances, to increase the SEIRA signal levels, it is highly important to (i) maximize the field overlap with the target sample and (ii) count and preserve the maximum number of photons interacting with the sample. The former is based on the fact that the enhancement in the absorption signal depends on the spatial overlap between the enhanced local electromagnetic fields and the adsorbed biomolecules in the vicinity of the nanostructures.[7] Traditional means of fabricating or immobilizing plasmonic nanoparticles on a solid dielectric substrate significantly limits the field overlap as a substantial portion of the enhanced nearfields reside in the substrate material, making it inaccessible for the biomolecules to be detected. Hence, studies have focused on engineering nanoparticle geometries and arrangements to maximize this overlap and therefore, the sensitivity.[7–14] Various antenna designs, including elongated shapes, e.g., rods,[23,46,47] split rings[48,49] or ring/disks,[7] have been utilized to improve SEIRA absorption signals. However, most of these structures are designed to be excited at the desired frequency only with a specific polarization of the incident light. Therefore in reference to issue (ii), such polarization-sensitive structures suffer from filteration of half of the incident light from an unpolarized source according to Malus' law,[50] thus failing to maximize the photon numbers interacting with biomolecules (see Supporting Information for our experimental results demonstrating this fact). Employing polarizers also results in high sensitivity to the alignment with respect to the incident light polarization. These limitations can be avoided by designing polarization-insensitive nanoantennas that are symmetric in all directions. Disk nanoantennas, which have been exploited in Near-IR and visible frequency ranges for RI-sensing applications,[51–55] are not polarization sensitive, but scaling their size for operation in Mid-IR spectral range (5–7 μm) is not trivial.

In this communication, we introduce a polarization-insensitive mid-IR nanoring antenna fabricated on a dielectric nanopedestal to provide maximum field overlap with the target biomolecules. Our suspended ring antenna design on pedestal is highly promising for ultrasensitive mid-IR vibrational spectroscopy specifically for applications associated with extremely low concentrations requiring high SNR. The resonance wavelength (λ_{res}) of the plasmonic ring antenna can be finely tuned by simply changing the circumference.[12,48,56–58] λ_{res} scales linearly with the ring radius (see Supporting Information), similar to the nanorod antennas where the resonance wavelength is scaled by the rod length.[23] Nanopedestals supporting the nanorings are fabricated through an isotropic fabrication

Dr. A. E. Cetin, D. Etezadi, Dr. H. Altug
Department of Electrical and Computer Engineering
Boston University
Boston, Massachusetts 02215, USA
E-mail: hatice.altug@epfl.ch
Dr. A. E. Cetin, D. Etezadi, Dr. H. Altug
Bioengineering Department
Ecole Polytechnique Federale de Lausanne (EPFL)
Lausanne CH-1015, Switzerland

DOI: 10.1002/adom.201400171

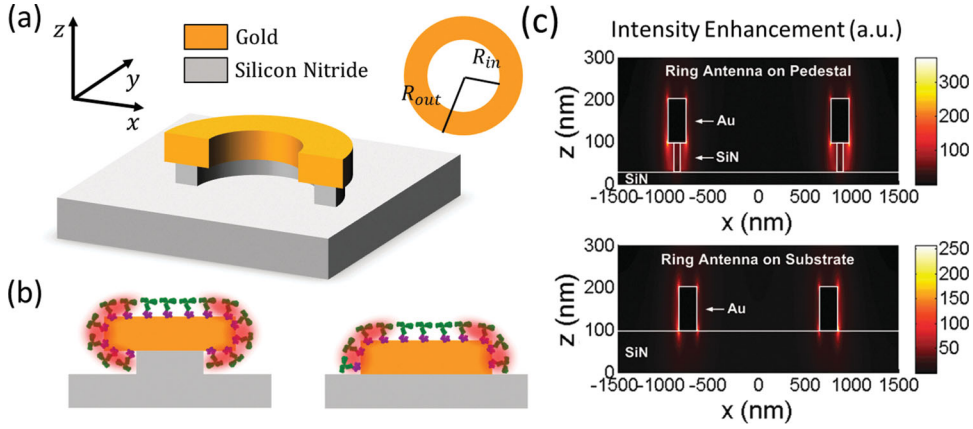

Figure 1. (a) Schematic view of the gold nanoring antenna on the silicon nitride nanopedestal. (b) Cross-sectional profile illustrating the availability of E-field hot spots for biomolecular bindings in the gold antenna on the silicon nitride pedestal and substrate. (c) Electric field intensity enhancement profile for the antenna systems on the nanopedestal and on substrate calculated at the spectral response engineered for the Amide I vibrational mode.

technique to provide maximum overlap between the target biomolecules and the plasmonic hot spots. Due to the symmetric nature of the antenna, we perform surface enhanced IR absorption spectroscopy without requirement for polarized incident light and sample alignment. With the engineered ring nanoparticles on the nanopedestal, we successfully detect Amide-I and II vibrational modes of a protein-antibody bilayer. Our experimental results demonstrate that the improvement in the absorption signals of vibrational modes is due to the stronger overlap between protein layers and optical fields. Using finite difference time domain (FDTD) simulations, we demonstrate a correlation between the absorption signal enhancement and the increment in the integral of the local electromagnetic fields over the protein layers, confirming our experimental results. The approach of introducing nanopedestals under the nanostructures for increasing the sensing volume, thus the SEIRA signal, can be applied to other antenna geometries, e.g., gap antennas.

To demonstrate the signal enhancement offered by our antenna design, we compare the absorption signals of the nanoantenna arrays on the nanopedestals and the substrate, covered with protein bilayer as used in the experiments. In FDTD simulations (Lumerical Solutions, Inc.), the dielectric constants of gold and adhesion layer (chromium) are taken from Palik's Handbook of Optical Constants of Solids.[59] **Figure 1**a and b show the schematic of the gold nanoring antenna design on the silicon nitride nanopedestal and substrate. As illustrated through the cross-sectional schematic in Figure 1b-left, our isotropic etching technique ensures that the tip ends of the nanoparticle and hence the full mode volume of the hot spots are available for biodetection. Based on our fabrication method, we optimize the substrate thickness and the antenna dimensions to provide a silicon nitride pedestal of 70 nm height while the silicon nitride nanoring width is 140 nm thinner than the gold nanoring width ($R_{out} - R_{in}$). Thicknesses of the gold antenna and bottom silicon nitride substrate are 100 nm and 260 nm, respectively. For the unit cell consisting of a single antenna, periodic boundary condition is used along the *x*- and *y*- directions (in order to have a collective periodic antenna behavior) and perfectly matched layer boundary condition is used along the direction of the illumination, *z*. Figure 1c is the cross-sectional profile of the near-field intensity enhancement distribution supported by the nanoring antennas. For the nanoring antenna on the nanopedestal, the effective refractive index in the vicinity of the array is smaller due to the partial removal of the silicon nitride substrate. Therefore, in order for these two antenna designs to support a plasmonic response at the same frequency, the antenna on the pedestal should be designed for larger dimensions (R_{in} = 750 nm and R_{out} = 950 nm) compared to the one on the substrate (R_{in} = 670 nm and R_{out} = 870 nm). According to FDTD simulations shown in Figure 1c, for the two antennas engineered for the same protein vibrational mode (Amide I), the antennas on the nanopedestals provide more than 1.4 times larger field enhancements. More importantly for the nanoantennas on the substrate, significant portion of the local fields is concentrated within the silicon nitride substrate, thus not accessible for the target biomolecules.

For calculating the absorption signals using these antennas, we numerically model a bilayer molecule consisting of protein A/G and Immunoglobulin (IgG) antibody. The real (black curve) and imaginary (green curve) parts of the modeled protein permittivity is shown in **Figure 2**a. In order to extract this model based on the experimentally obtained complex permittivity of the protein bilayer (obtained by infrared reflection absorption spectroscopy), we use a Lorentz model where we fit 3 oscillators to the experimental data using following equation:

$$\varepsilon_{bilayer} = \varepsilon_{\infty} + \sum_{i=1}^{3} \frac{S_i}{\omega_{Pi}^2 - \omega^2 - j\omega\gamma_{Pi}} \quad (1)$$

Here, ε_{∞} is the high frequency constant term, ω_p is the oscillator resonance frequency, γ_p is the damping frequency and *S* is the oscillator strengths. The values for the 3 oscillators are ε_{∞} = 2.1901, $\omega_{P1} = 3.12 \times 10^{14}$ (rad/s), $\omega_{P2} = 2.90 \times 10^{14}$ (rad/s), $\omega_{P3} = 2.73 \times 10^{14}$ (rad/s) and $\gamma_{P1} = 0.98 \times 10^{13}$ (rad/s), $\gamma_{P2} = 1.02 \times 10^{13}$ (rad/s), $\gamma_{P3} = 0.95 \times 10^{13}$ (rad/s) and $S_1 = 2.6 \times 10^{27}$ (rad/s)^2, $S_2 = 1.8 \times 10^{27}$ (rad/s)^2, $S_3 = 0.5961 \times 10^{27}$ (rad/s)^2. In Figure 2, red line denotes Amide I (at ~6025 nm) corresponding to C=O stretching vibration and blue line denotes Amide II (at ~6562 nm) corresponding to C–N–H bending and

Adv. Optical Mater. **2014**,
DOI: 10.1002/adom.201400171

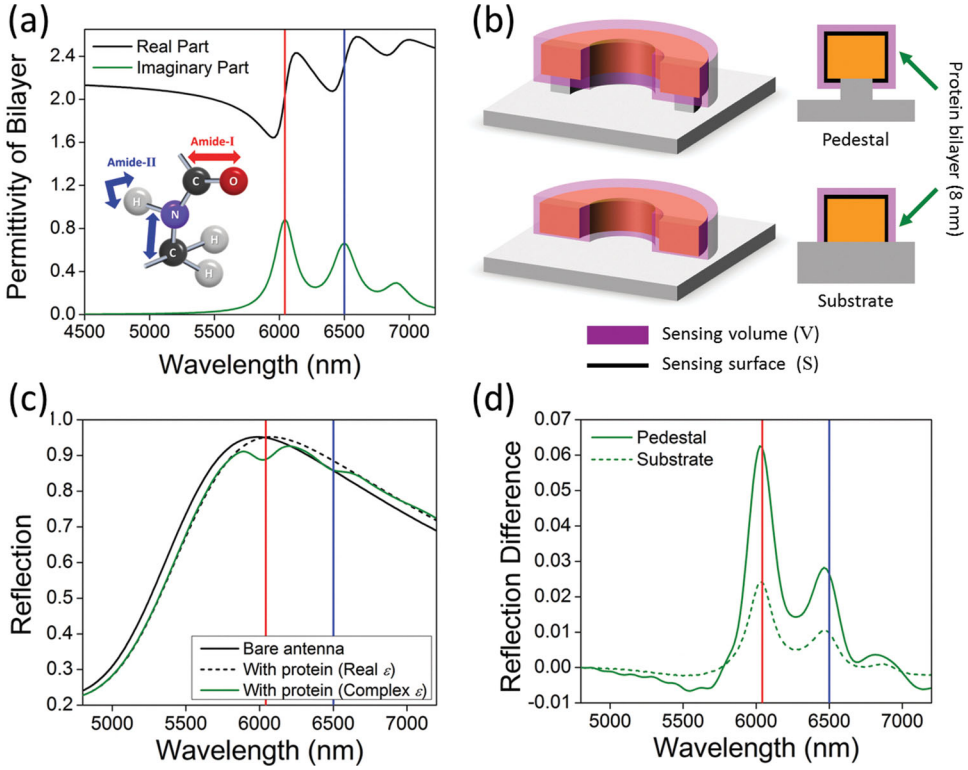

Figure 2. (a) Real (black curve) and Imaginary (green curve) parts of the modeled permittivity function for the protein bilayer (A/G + IgG). Figure inset schematically illustrates the Amide I and II vibrational modes of the protein back bone. (b) Schematic illustration of the protein bilayer with a thickness of ~8 nm on the surface of the gold antenna. In the figure, the purple color representing the protein bilayer shows the sensing volume and the black line shows the sensing surface. (c) Calculated bare reflection spectrum of the nanoring antenna on the nanopedestal with no protein layer (black curve) and after the coating of the protein bilayer with real (black dashed curve) and complex (green curve) permittivity. (d) Calculated reflection difference spectra for the nanorings antennas on the silicon nitride nanopedestal (green curve) and substrate (dashed green curve) demonstrating the protein vibrational signatures. In the figures, the red and blue lines show the Amide I and II vibrational modes of the protein bilayer, respectively. The corresponding device parameters: for nanoring antenna on the substrate: R_{in} = 670 nm and R_{out} = 870 nm and for nanoring antenna on the pedestal: R_{in} = 750 nm and R_{out} = 950 nm, and the period of the array is 3 μm.

C–N stretching vibrations (schematically illustrated in the figure inset). Here, the third vibrational signature observed in longer wavelengths (at ~6905 nm) is due to the weak Amide III band and out of focus for this article. For our numerical calculations, we design the antennas primarily for Amide I vibrational band. In FDTD simulations, we use a protein bilayer with a thickness of ~8 nm. The protein layer thickness is experimentally characterized through ellipsometry measurements (Woollam).[60] Our surface chemistry protocols ensure that the protein bilayer only covers the surface of the antennas due to the specific binding of protein A/G monolayer to the metal surface. This protein coverage is modeled by defining an 8 nm thick dielectric layer covering only the gold surface (illustrated in Figure 2b).

Detection of the protein vibrational signatures is achieved through monitoring the change in the reflection spectrum of the nanoring antenna after adding the biomolecules. Figure 2c shows the response of the ring antenna on the nanopedestal before (black curve) and after (green curve) the protein binding. As shown in Figure 2c, for the nanoantenna on the nanopedestal, vibrational signatures are clearly observed as spectral dips in the reflection response due to the Amide I and II absorption bands. Here, in addition to the spectral dips due to the protein absorption resulting from the imaginary part of the complex protein permittivity, we observe a red-shift in the antenna response which originates from the array sensitivity to the real part of the protein permittivity.[61] In order to take this shift into account, we replace the initial response (black curve labeled with "Bare antenna") with the reflection spectrum from the antenna array covered with a reference material with the real part of the refractive index of the protein bilayer and zero absorption (no imaginary part). This response (black dashed curve), labeled as "With protein (Real ε)", overlaps with the response of the antennas covered with the protein bilayer model (denoted with a green curve).

Figure 2d shows the reflection difference spectrum calculated from antennas engineered for Amide I vibrational band, for the antenna on the silicon nitride nanopedestal (green curve) and on the silicon nitride substrate (dashed green curve). The spectrum is calculated from the difference between the ring antenna responses before (denoted with a black dashed curve in Figure 2c) and after (denoted with a green curve in Figure 2c) adding the protein bilayer, $\Delta R = R_{With\ protein(Real\ \varepsilon)} - R_{With\ protein(Complex\ \varepsilon)}$. The antenna arrays on the nanopedestal yield a reflection difference as large as 0.06254 (corresponding to 33 mOD absorption signal) at the Amide I band. This value corresponds to an additional enhancement in the reflection difference as large as

Table 1. Comparison of the available sensing surface S, integral of the nearfield intensity enhancement (a.u.) over the sensing volume $V(\mathrm{nm}^3) = S(\mathrm{nm}^2) \times 8\mathrm{nm}$, calculated reflection difference corresponding to absorption signals of Amide I vibrational mode for the gold nanoring antennas on the silicon nitride substrate and nanopedestal.

	Available Sensing Surface, S [nm^2]	$\iiint_{V(\mathrm{nm}^3)} I(x,y,z)dV$	Calculated Reflection Difference for Amide I
Antenna on Pedestal	2.9518×10^6	4.0574×10^7	0.06254
Antenna on Substrate	1.7593×10^6	1.5473×10^7	0.02397

~2.6 times compared to the ring antennas fabricated directly on the dielectric substrate (0.02397 reflection difference). Even though the antenna is designed for Amide I vibrational mode and the mode supported by the nanoring is blue-shifted from the Amide II, it still benefits from the accessible local electromagnetic fields, yielding an absorption signal as large as 15 mOD. On the other hand, for the antenna on substrate, the reflection difference values correspond to absorption signals of only 8 and 4 mOD for Amide I and II bands, respectively.

The enhancement in the absorption signal with the use of the nanopedestal can be explained by considering the improved sensing volume and the large local electromagnetic fields associated with it. For a quantitative comparison, we calculate the integral of the local electromagnetic fields over the protein bilayer region. For the nanopedestal, as the silicon nitride substrate under the antenna is partially removed, the available binding region for sensing is larger. In **Table 1**, we calculate the sensing surface, S as schematically shown in Figure 2b. The ring antennas on the nanopedestal support ~1.68 times larger sensing surface compared to the ones on the substrate. Next, we calculate the integral of the enhanced fields over the sensing volume (V) by considering the fact that the protein molecules form an 8 nm thick bilayer on the gold surface, i.e., $V(\mathrm{nm}^3) = S(\mathrm{nm}^2) \times 8\mathrm{nm}$. As shown in Table 1 for Amide I, the nanopedestal design enables ~2.6 times larger integral value due to the improved sensing surface and higher local electromagnetic fields. This value is in agreement with the previously presented enhancement in the reflection difference (~2.6 times in Figure 2d) as shown in the last column of Table 1.

For experimental demonstration, we fabricate nanoring antennas on the silicon nitride nanopedestals by adding an etching step after the fabrication of the nanoantennas on the substrate. **Figure 3**a illustrates the manufacturing steps. We start with a 400 nm thick silicon nitride membrane supported by silicon. The fabrication process of the silicon nitride membranes is described in supporting information. Thin silicon nitride substrate enables transmission and reflection measurements in Mid-IR spectral range with almost no optical loss. (i) We first perform E-beam lithography using a positive resist, Polymethyl methacrylate (950PMMA A5, MICROCHEM). (ii) After development using methyl isobutyl ketone and isopropyl alcohol (MIBK-IPA, 1:3) solution, we deposit a thin layer of chromium serving as an adhesion layer, and 100 nm gold. (iii) We then perform a lift-off process using acetone and IPA to remove the gold from the unexposed surface resulting in gold nanoantennas on the silicon nitride substrate. (iv) Finally, in order to suspend the nanoparticles on the nanopedestals and expose their tip ends, we etch the silicon nitride layer using hydrofluoric acid solution (HF concentrated 48%). Here, a controlled wet-etching procedure is critical to sufficiently undercut

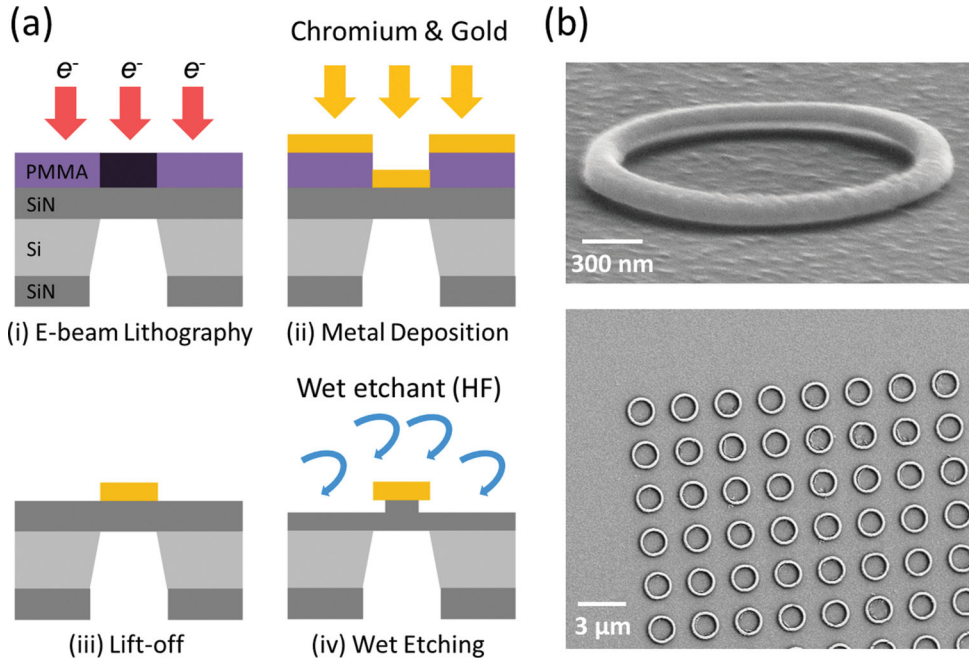

Figure 3. (a) Fabrication process of the gold nanoantennas on (iii) the silicon nitride (SiN) substrate and (iv) on nanopedestal with isotropic wet-etching process. (b) SEM images of the gold nanoring antennas on nanopedestal. The corresponding device parameters are: R_{in} = 750 nm, R_{out} = 950 nm, and the period of the array is 3 µm.

Adv. Optical Mater. **2014**,
DOI: 10.1002/adom.201400171

the silicon nitride substrate while avoiding the removal of nanoantennas due to over-etching. Using isotropic wet-etching process, we remove silicon nitride by ~70 nm along all directions. After the etching procedure, the thickness of the remaining silicon nitride membrane is 260 nm and the height of the pedestal underneath the antenna is 70 nm. The width of the silicon nitride nanoring pedestal is 140 nm thinner compared to that of the gold nanoring antenna ($R_{in}(\text{silicon nitride}) = 820\,\text{nm}$ and $R_{out}(\text{silicon nitride}) = 880\,\text{nm}$). Figure 3b shows the scanning electron microscope (SEM) image of the antennas on the pedestal with R_{in} = 750 nm, R_{out} = 950 nm and array period of 3 μm, demonstrating that the silicon nitride layer is well-etched and the gold nanoantennas are intact and uniform. Our fabrication method, yielding suspended nanoparticles, can be applied for other antenna geometries and substrates with appropriate etching chemistry.

In this section, we experimentally demonstrate the advantage of the nanopedestals in SEIRA measurement. Reflection response of the nanoring antennas is collected using a Fourier transform infrared spectrometer (Bruker, IFS 66/s) coupled to an infrared microscope (Bruker, Hyperion 1000). The spectra are collected at a resolution of 4 cm^{-1} and consist of 256 scans co-added with a mirror repetition rate of 40 kHz. Spectroscopic scans are performed under a dry air purged environment to eliminate atmospheric water vapor absorption in the spectral region of interest. **Figure 4**a and b show the experimental spectral response of the nanoring antennas on the silicon nitride substrate and on nanopedestals, respectively. The antennas support spectrally narrow plasmon excitations[62] around 6 μm covering specifically Amide I and II vibrational modes of the protein back bone for the bilayer (A/G from Pierce and goat IgG from Sigma). As confirmed experimentally, the spectral location of the plasmonic mode can be controlled with the radius of the ring. Here, the additional spectral feature at ~2100 nm is associated with silicon nitride substrate and does not depend on the antenna array. Figure 4c shows the initial response of the nanoring antenna on the silicon nitride pedestal labeled with "Bare antenna" (black curve). After introducing the protein bilayer, in addition to the spectral dips corresponding to the absorption, (green line) labeled with "With protein (Complex ε)", we also observe a red-shift in plasmonic resonance due to the real part of the protein permittivity which increases the effective refractive index of the surrounding environment as explained earlier. In order to take this shift into account, we utilize a polynomial fitting procedure and obtain a shifted spectrum (dashed black curve) labeled with "With protein (Real ε)" for calculation of the absorption signal.[23] Figure 4d shows the experimental reflection difference spectra ($\Delta R = R_{With\ protein(Real\,\varepsilon)} - R_{With\ protein(Complex\,\varepsilon)}$) of the ring antennas on the silicon nitride nanopedestal (green curve) and substrate (dashed green curve). Here, due to the fabrication tolerance, the resonance peaks of the bare antenna responses (Figure 4a,b) are not exactly overlapping with the Amide I band. This mismatch further increases by the spectral

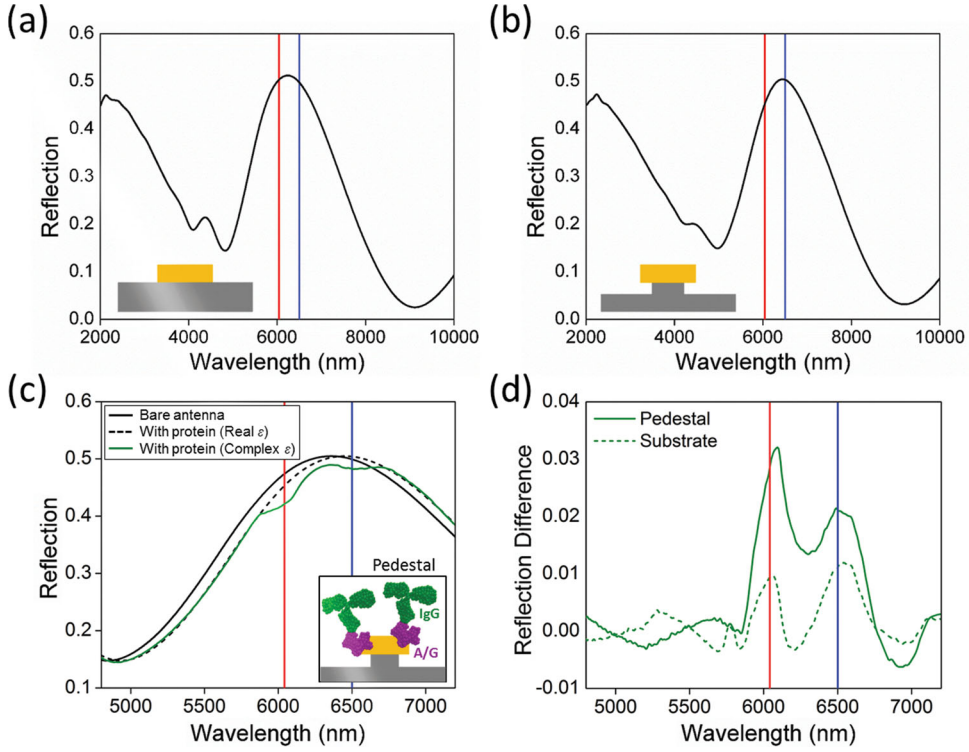

Figure 4. Experimental reflection spectra for the gold nanoring antennas on the silicon nitride (a) substrate and (b) nanopedestal. (c) Experimental reflection spectra of the nanoring antenna on the nanopedestal before (black curve) and after modification (dashed black curve), and after the coating of the protein bilayer (green curve). (d) Experimental reflection difference spectra for the nanoring antennas on the silicon nitride nanopedestal (green curve) and substrate (dashed green curve) demonstrating the protein vibrational signatures. In figures, red and blue lines show Amide I and II vibrational modes of the protein bilayer, respectively. The corresponding device parameters: for nanoring antenna on the substrate: R_{in} = 670 nm and R_{out} = 870 nm, for nanoring antenna on the nanopedestal: R_{in} = 750 nm and R_{out} = 950 nm, and the period of the array is 3 μm.

red-shift after the bilayer binding. Even though the antenna system on the substrate favors the plasmonic excitations more, the later one still supports larger absorption signal (green curve in Figure 4d) due to its highly accessible local electromagnetic fields. We determine that the antennas on the nanopedestals give 30 mOD and 18 mOD absorption signals at the Amide I and II bands, respectively, while the antennas on substrate provide only 3 mOD for Amide I and 7 mOD for Amide II. These experimental results are in good agreement with our calculations shown in Figure 2d. It is also interesting to note that, as the response of the antenna system on the substrate better overlaps with the Amide II band after the spectral shift, absorption signal obtained from the antenna for this band is stronger than Amide I band (green dashed curve in Figure 4d).

In conclusion, we successfully introduce plasmonic nanoring antennas fabricated on dielectric nanopedestals which increase the sensing signals by supporting highly accessible electromagnetic fields. Our symmetric nanoring antennas eliminate the need for the use of polarizers in the measurements and provide an alignment insensitive design that can utilize the total power of the IR source. By incorporating an absorbing protein bilayer in FDTD simulations, we are able to calculate the absorption signals of the modeled vibrational protein bands in a good agreement with our experiments. We also numerically demonstrate a correlation between the enhancement in the absorption signal and the improvement in the accessibility of the local electromagnetic fields over the protein layers. In order to experimentally realize suspending nanoparticles on thin nanopedestals, we introduce an isotropic etching method ensuring significant undercutting below the nanoparticle antennas, hence fully exposing the spatial regions where the field enhancement is largest. This fabrication method is applicable to antennas of other shapes with only a single additional fabrication step. By providing higher sensitivity, these nanoring antennas on nanopedestals are highly advantageous for applications requiring high SNR.

Supporting Information

Supporting Information is available from the Wiley Online Library or from the author.

Acknowledgements

Dr. A. E. Cetin and D. Etezadi contributed equally to this work. Altug Research Group acknowledges National Science Foundation (NSF) CAREER Award and Presidential Early Career Award for Scientist and Engineers ECCS-0954790, Office of Naval Research (ONR) Young Investigator Award 11PR00755–00-P00001, NSF Engineering Research Center on Smart Lighting EEC-0812056 and Ecole Polytechnique Federale de Lausanne.

Received: April 17, 2014
Revised: May 21, 2014
Published online:

[1] F. Huth, M. Schnell, J. Wittborn, N. Ocelic, R. Hillenbrand, *Nat. Mater.* **2011**, *10*, 352.
[2] P. Mühlschlegel, H. J. Eisler, O. J. F. Martin, B. Hecht, D. W. Pohl, *Science* **2005**, *308*, 1607.
[3] A. V. Kabashin, P. Evans, S. Pastkovsky, W. Hendren, G. A. Wurtz, R. Atkinson, R. Pollard, V. A. Podolskiy, A. V. Zayats, *Nat. Mater.* **2009**, *8*, 867.
[4] S. Lal, S. Link, N. J. Halas, *Nat. Photonics* **2007**, *1*, 641.
[5] R. Zia, *Nat. Photonics* **2008**, *2*, 213.
[6] D. O'Connor, A. V. Zayats, *Nat. Nanotechnol.* **2010**, *5*, 482.
[7] A. E. Cetin, H. Altug, *ACS Nano* **2012**, *6*, 9989.
[8] A. E. Cetin, A. A. Yanik, C. Yilmaz, S. Somu, A. A. Busnaina, H. Altug, *Appl. Phys. Lett.* **2011**, *98*, 111110.
[9] B. Luk'yanchuk, N. I. Zheludev, S. A. Maier, N. J. Halas, P. Nordlander, H. Giessen, C. T. Chong, *Nat. Mater.* **2010**, *9*, 707.
[10] V. J. Sorger, N. Pholchai, E. Cubukcu, R. F. Oulton, P. Kolchin, C. Borschel, M. Gnauck, C. Ronning, X. Zhang, *Nano Lett.* **2011**, *11*, 4907.
[11] S. A. Maier, H. A. Atwater, *J. Appl. Phys.* **2005**, *98*, 011101.
[12] V. Liberman, C. Yilmaz, T. M. Bloomstein, S. Somu, Y. Echegoyen, A. Busnaina, S. G. Cann, K. E. Krohn, M. F. Marchant, M. A. Rothschild, *Adv. Mater.* **2010**, *22*, 4298.
[13] E. M. Larsson, J. Alegret, M. Kall, D. S. Sutherland, *Nano Lett.* **2007**, *7*, 1256.
[14] Y. B. Zheng, Y. W. Yang, L. Jensen, L. Fang, B. K. Juluri, A. H. Flood, P. S. Weiss, J. F. Stoddart, T. J. Huang, *Nano Lett.* **2009**, *9*, 819.
[15] N. Liu, L. Langguth, T. Weiss, J. Kastel, M. Fleischhauer, T. Pfau, H. Giessen, *Nat. Mater.* **2009**, *8*, 758.
[16] H. Im, N. C. Lindquist, A. Lesuffleur, S. H. Oh, *ACS Nano* **2010**, *4*, 947.
[17] J. B. Lassiter, H. Sobhani, J. A. Fan, J. Kundu, F. Capass, P. Nordlander, N. J. Halas, *Nano Lett.* **2010**, *10*, 3184.
[18] V. K. Valev, B. De Clercq, C. G. Biris, X. Zheng, S. Vandendriessche, M. Hojeij, D. Denkova, Y. Jeyaram, N. C. Panoiu, Y. Ekinci, A. V. Silhanek, V. Volskiy, G. A. E. Vandenbosch, M. Ameloot, V. V. Moshchalkov, T. Verbiest, *Adv. Mater.* **2012**, *24*, 208.
[19] H. Wei, D. Ratchford, X. Li, H. Xu, C. K. Shih, *Nano Lett.* **2009**, *9*, 4168.
[20] E. B. Flagg, A. Muller, J. W. Robertson, S. Founta, D. G. Deppe, M. Xiao, W. Ma, G. J. Salamo, C. K. Shih, *Nat. Phys.* **2009**, *5*, 203.
[21] H. Caglayan, I. Bulu, M. Loncar, E. Ozbay, *Opt. Lett.* **2009**, *34*, 88.
[22] J. Hao, J. Wang, X. Liu, W. J. Padilla, L. Zhou, M. Qiu, *Appl. Phys. Lett.* **2010**, *96*, 251104.
[23] R. Adato, A. A. Yanik, J. J. Amsden, D. L. Kaplan, F. G. Omenetto, M. K. Hong, S. Erramilli, H. Altug, *Proc. Natl. Acad. Sci. USA* **2009**, *106*, 19227.
[24] A. A. Yanik, A. E. Cetin, M. Huang, A. Artar, S. H. Mousavi, A. Khanikaev, J. H. Connor, G. Shvets, H. Altug, *Proc. Natl. Acad. Sci. USA* **2011**, *108*, 11784.
[25] A. A. Yanik, M. Huang, O. Kamohara, A. Artar, T. W. Geisbert, J. H. Connor, H. Altug, *Nano Lett.* **2010**, *10*, 4962.
[26] T. Y. Chang, M. Huang, A. A. Yanik, H. Y. Tsai, P. Shi, S. Aksu, M. F. Yanik, H. Altug, *Lab Chip* **2011**, *11*, 3596.
[27] A. D. McFarland, R. P. Van Duyne, *Nano Lett.* **2003**, *3*, 1057.
[28] B. Pettinger, B. Ren, G. Picardi, R. Schuster, G. Ertl, *Phys. Rev. Lett.* **2004**, *92*, 96101.
[29] D. Lasne, G. A. Blab, S. Berciaud, M. Heine, L. Groc, D. Choquet, L. Cognet, B. Lounis, *Biophys. J.* **2006**, *91*, 4598.
[30] C. Sonnichsen, B. M. Reinhard, J. Liphardt, A. P. Alivisatos, *Nat. Biotechnol.* **2005**, *23*, 741.
[31] T. Endo, K. Kerman, N. Nagatani, H. M. Hiepa, D. K. Kim, Y. Yonezawa, K. Nakano, E. Tamiya, *Anal. Chem.* **2006**, *78*, 6465.
[32] D. A. Stuart, J. M. Yuen, N. Shah, O. Lyandres, C. R. Yonzon, M. R. Glucksberg, J. T. Walsh, R. P. Van Duyne, *Anal. Chem.* **2006**, *78*, 7211.
[33] K. Kneipp, Y. Wang, H. Kneipp, L. T. Perelman, I. Itzkan, R. R. Dasari, M. S. Feld, *Phys. Rev. Lett.* **1997**, *78*, 1667.

[34] J. Kundu, F. Le, P. Nordlander, N. J. Halas, *Chem. Phys. Lett.* **2008**, *452*, 115.
[35] A. Kinkhabwala, Z. Yu, S. Fan, Y. Avlasevich, K. Mullen, W. E. Moerner, *Nat. Photonics* **2009**, *3*, 654.
[36] I. M. Pryce, Y. A. Kelaita, K. Aydin, R. M. Briggs, H. A. Atwater, *ACS Nano* **2011**, *10*, 8167.
[37] A. E. Cetin, A. F. Coskun, B. C. Galarreta, M. Huang, D. Herman, A. Ozcan, H. Altug, *Light. Sci. Appl.* **2014**, *3*, e122.
[38] C. Wu, A. B. Khanikaev, R. Adato, N. Arju, A. A. Yanik, H. Altug, G. Shvets, *Nat. Mater.* **2012**, *11*, 69.
[39] B. Zachhuber, C. Gasser, G. Ramer, E. H. Chrysostom, B. Lendl, *Appl. Spectrosc.* **2012**, *66*, 875.
[40] K. J. Ewing, B. Lerner, *Appl. Spectrosc.* **2001**, *55*, 407.
[41] K. J. Ewing, D. Gibson, J. Sanghera, *Anal. Chem.* **2013**, *85*, 9508.
[42] S. Aksu, A. A. Yanik, R. Adato, A. Artar, M. Huang, H , Altug. *Nano Lett.* **2010**, *10*, 2511.
[43] R. Adato, H. Altug, *Nat. Commun.* **2013**, *4*, 1–10.
[44] M. Osawa, K. Ataka, K. Yoshi, Y. Nishikawa, *Appl. Spectrosc.* **1993**, *47*, 1497.
[45] F. Ballout, H. Krassen, I. Kopf, K. Ataka, E. Bründermann, J. Heberle, M. Havenith, *Phys. Chem. Chem. Phys.* **2011**, *13*, 21432.
[46] F. Neubrech, A. Pucci, T. W. Cornelius, S. Karim, A. Garcia-Etxarri, J. Aizpurua. *Phys. Rev. Lett.* **2008**, *101*, 157403.
[47] F. Neubrech, A. Pucci, *IEEE J. Sel. Top. Quantum Electron.* **2013**, *19*, 4600809.
[48] B. Lahiri, A. Z. Khokhar, R. M. De La Rue, S. G. McMeekin, N. P. Johnson, *Opt. Express* **2009**, *17*, 1107.
[49] S. Cataldo, J. Zhao, F. Neubrech, B. Frank, C. Zhang, P. V. Braun, H. Giessen, *ACS Nano* **2012**, *6*, 979.
[50] E. Hecht, *Optics*, Addison-Wesley, New York, USA **1990**.
[51] H. Jiang, T. Manifar, A. Bakhtazad, H. Hojjati, J. Sabarinathan, S. Mittler, *J. Appl. Phys.* **2013**, *113*, 224306.
[52] M. A. Otte, M. C. Estevez, L. G. Carrascosa, A. B. Gonzalez-Guerrero, L. M. Lechuga, B. Sepulveda, *J. Phys. Chem. C* **2011**, *115*, 5344.
[53] H. Jiang, T. Li, E. Ertorer, J. Yang, J. Sabarinathan, S. Mittler, *Sens. Actuators A* **2013**, *189*, 474.
[54] S. Chen, M. Svedendahl, M. Kall, L. Gunnarsson, A. Dmitriev, *Nanotechnology* **2009**, *20*, 434015.
[55] G. Barbillon, J. L. Bijeon, J. Plain, P. Royer, *Thin Solid Films* **2009**, *517*, 2997.
[56] D. Ahmadian, Ch. Ghobadi, J. Nourinia, *Opt. Quant. Electron.* **2013**, *0306–8919*, 1.
[57] C. Huang, J. Ye, S. Wang, T. Stakenborg, L. Lagae, *Appl. Phys. Lett.* **2012**, *100*, 173114.
[58] K. Lodewijks, W. V. Roy, G. Borghs, L. Lagae, P. V. Dorpe, *Nano Lett.* **2012**, *12*, 1655.
[59] E. D. Palik, *Handbook of Optical Constants of Solids*, Academic, Orlando, USA **1985**.
[60] R. Adato, A. A. Yanik, C.-H. Wu, G. Shvets, H. Altug, *Opt. Express* **2010**, *18*, 4526.
[61] V. Liberman, R. Adato, T. H. Jeys, B. G. Saar, S. Erramilli, H. Altug, *Opt. Express* **2012**, *20*, 11953.
[62] E. Prodan, C. Radloff, N. J. Halas, P. Nordlander, *Science* **2003**, *302*, 419.